Bioactive Materials 5 (2020) 133–141

Contents lists available at ScienceDirect

Bioactive Materials

journal homepage: http://www.keaipublishing.com/biomat

Influence of stamping on the biodegradation behavior of Mg–2Zn-0.5Nd (ZN20) sheet

Iniobong P. Etim[a,b], Wen Zhang[a,b], Lili Tan[a,*], Ke Yang[a,**]

[a] Institute of Metal Research, Chinese Academy of Sciences, Shenyang, 110016, China
[b] School of Materials Science and Engineering, University of Science and Technology of China, Shenyang, 110016, China

ARTICLE INFO

Keywords:
Texture
Degradation rate
Crystallographic orientation
Stamping
Annealing
Twin
Deformation

ABSTRACT

Stamping processing is commonly used to form medical devices and implant. However, for biodegradable Mg alloy, the stamping will influence the degradation behavior because of the change in microstructure after stamping. So in this study, the As-rolled Mg–2Zn-0.5Nd alloy (ZN20) was processed by stamping. The microstructure, crystallographic orientation and corrosion performance of this processing method was investigated to reveal the influence of the stamping process on the degradation rate of Rolled Mg–2Zn–Nd (ZN20). The degradation rate was measured by immersion of the Mg–2Zn-0.5Nd alloy in simulated body fluid using Electrochemical Impedance Spectroscopy, Potentiodynamic polarization and mass loss. The in vitro degradation result shows that the degradation rate of the Rolled Mg–2Zn-0.5Nd increased from 0.2 mm/year to 0.5 mm/year after stamping processing. The result reveals that the activation of the $\{10\bar{1}2\}$tension twin during stamping can remarkably weaken the {0001} basal texture and have a significant influence on the corrosion rate of Stamped Mg–2Zn-0.5Nd sheet. After removing the deformation by annealing, the degradation rate was reduced to 0.15 mm/year. This work is expected to prompt better microstructural design of biomedical Mg in order to control its degradation behavior for biomedical application.

1. Introduction

In recent years, the development of biodegradable material has attracted a great deal of attention. The concept of applying biodegradable implants is to aid tissue revival and healing through the degradation of specific material and replacement of current implants with nearby tissue [1]. Compared with other biodegradable materials like polymers, ceramics and bioactive glasses, biodegradable metallic materials exhibit enhanced behavior in load bearing applications because of their higher tensile strength and toughness [1–4]. Magnesium based alloys stands out among biodegradable metallic materials because they are physiologically compatible, biodegradable in human body and can stimulate bone formation [1–3]. As a light weight metal the elastic modulus of Mg (44 GPa) is closer to natural bone (17 GPa) than traditional metallic implant materials like stainless steel, titanium and cobalt chromium alloys [5]. The fracture toughness and yield strength of Mg is also more comparable to the natural bone than other metallic biomaterials like Ti alloys [1,2].

Several elements such as Al, Zn, Mn, Ca, Sr, Li, Si, rare earth element and so on have been alloyed with Mg to improve its strength and plasticity [5–9]. Among the various magnesium alloys, Mg alloys containing Rare-earth element (RE) have received considerable attention in recent years due to their better mechanical properties and corrosion resistance [10–12]. Sietz et al. [13] reported that Mg–2Nd alloy had a unique combination of high elongation ratios with low yield strength and low corrosion rate. Mg–2Zn-0.5Nd (ZN20) was recently developed by our group and has shown good corrosion resistance and potentials for coronary stent application [58]. Zn is one of the essential nutritional elements for the human body. A small amount of Zn improves the strength of Mg alloys due to solid solution strengthening. Solid solution Nd could improve the matrix potential and decrease the galvanic corrosion between the matrix and the second phases. Nd is also beneficial to the corrosion resistance of Mg due to its similar potential to Mg and studies show that it doesn't exhibit cell toxicity [14–16].

However, its poor corrosion resistance and high degradation rate not only affects the service duration of implant before healing but decreases its mechanical properties which lead to failure [5,17,18]. Therefore, it is important for the corrosion resistance of magnesium

Peer review under responsibility of KeAi Communications Co., Ltd.
* Corresponding author.
** Corresponding author.
E-mail addresses: lltan@imr.ac.cn (L. Tan), kyang@imr.ac.cn (K. Yang).

https://doi.org/10.1016/j.bioactmat.2020.01.009
Received 6 November 2019; Received in revised form 15 January 2020; Accepted 20 January 2020

alloy to be enhanced for better biomedical application [1,5,19]. Several approaches used to improve the corrosion properties of magnesium include alloying [20,21], coating [22,23], processing technologies [24,25] and crystallographic structure modification [26–30]. Knowledge on the relationship between crystallographic orientation and corrosion rate is very important because it can provide guide on the optimization process to obtain the desirable texture for corrosion resistance. These processing technologies often change the microstructure which in turn can change the corrosion behavior of Mg alloy [31–34]. Liu et al. [30] reported that the lowest corrosion rate for a single pure Mg crystal in a 0.1 M HCl solution was obtained at the basal plane. Abuleil et al. [35] reported that the extrusion process increased the corrosion resistance of Mg–Sn alloy. The process of stamping not only changes the microstructure but also modifies the grain size, the refinement and rearrangement of the βphase and texture. In addition, it has been discovered that controlling crystallographic texture can remarkably influence the corrosion of Mg alloys [27,28,30,36–39]. Generally, a densely packed crystallographic plane (i.e. {0001} basal plane) exhibits a slower corrosion rate than a loosely packed plane due to its higher atomic co-ordination and stronger atomic bonding [40]. Song et al. reported that the corrosion rate of a cross-sectional surface mainly made up of $\{10\bar{1}0\}$ and $\{11\bar{2}0\}$ prism planes was about 8.4 times higher than that of a rolling surface consisting of {0001} basal planes [27]. The strong crystallographic texture in Mg alloys formed during severe plastic deformation such as rolling [27,28] and extrusion process [41,42], makes corrosion anisotropy in as-rolled and as-extruded Mg alloy [27,28,36,37,41,42], magnesium single crystals [38] and pure Mg [39] unavoidable.

For a long time, the medical industry felt that most medical devices and components required machining. But today's technology allows for effective stamping and micro-stamping of even some of the smallest and most complex parts for medical field application. Stamping process is very effective for processing several medical parts and devices, such as surgical instruments like jaw housings used for laparoscopic surgery, biomedical implants in form of bracelets, clamps and clips. The stamping technology makes it very easy and efficient to mass-produce these tiny devices. The knowledge of the effect of this process on the microstructure and corrosion property of biodegradable Mg alloy is very important, but seldom investigated. In this present work, we investigate the influence of stamping processing on the microstructure and biodegradation property of As-rolled Mg–2Zn-0.5Nd.

2. Experimental details

2.1. Material preparation

Mg–2Zn-0.5Nd as-cast plates 400 × 150 x 2 were prepared from pure Mg (99.957 wt %), pure Zn (99.99 wt %) and Mg–20Nd (99.99 wt %) master alloy in an electric resistance furnace under protection of an SF_6 and CO_2 gas mixture in a graphite crucible. Homogenization treatment was carried out at 300 ˚C for 3 h on the as-cast plates, and then uniformly rolled at a speed of 2 mm/min. The Rolled sheets of 0.7 mm thickness were obtained from the 2 mm thick plate after 2 h preheating at 300 ˚C. The rolled sheets were placed in a blank form into a stamping press where a tool and die surface transformed the rolled sheet into circular samples of 10 mm diameter, as shown in Fig. 1.The stamping was carried out at a force of 3 KN and speed of 200 mm/min. Finally, the stamped samples were annealed at 400 ˚C for 3 h. The rolled, stamped and annealed samples were named Rolled ZN20, Stamped ZN20 and HT-stamped ZN20 respectively. The chemical compositions of the Mg–2Zn-0.5Nd alloys are listed in Table 1.

2.2. Microstructure characterization

Specimens of Φ 10 × 0.5 mm of rolled, stamped and HT-stamped samples were prepared by standard metallographic techniques and

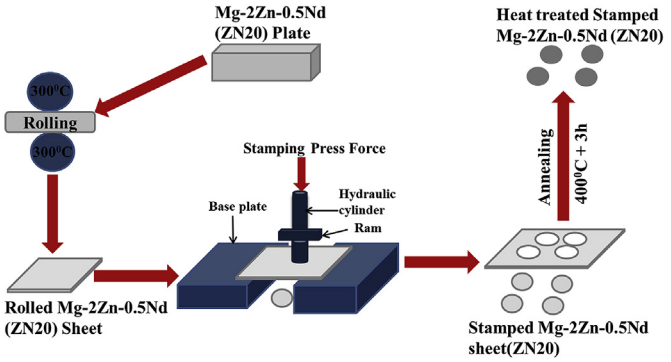

Fig. 1. Schematic diagram illustrating the stamping and heat treatment Process of Mg–2Zn-0.5Nd.

Table 1
Chemical composition of experimental ZN20 (wt.%).

Zn	Nd	Fe	Co	Ni	Cu	Mg
1.84	0.52	0.005	< 0.003	< 0.003	< 0.003	Bal.

were etched in a solution containing 6 g picric, 10 ml acetic, 10 ml water and 70 ml ethanol. Microstructure observation was performed using an optical microscope (OLYMPUS-GX7). The microstructure evolution and pole figures of the specimens were obtained by EBSD analysis using an HKL channel 5 systems (equipped in FEI Nova 400 FEG-SEM).

2.3. Immersion test

Specimens (Φ10 mm × 0.5 mm) were immersed in Hank's solution [43] for 14 days. The ratio of specimen surface area (cm^2) to solution volume (mL) was 1.25. The solution was changed each day to keep the solution fresh for the 14 days period. The pH value was measured for 14 days. After immersion, the specimens were cleaned in chromium trioxide solution to remove the corrosion product and corrosion rate was calculated using equation (1). The corrosion morphologies of the samples were observed by camera and scanning electron microscope (SEM).

$$\text{Corrosion Rate} = (\ K\times W)/(\ A\times T\times D) \quad (1)$$

Where the coefficient $K = 8.76 \times 10^4$, W is the weight loss (g), A is the sample area exposed to solution (cm^2), T is the exposure time (h) and D is the density of the material (g/cm^3).

2.4. Electrochemical test

Electrochemical measurement in Hank's solution [25] was carried out on several samples with surface area of 0.785 cm^2 at 37 ˚C using a Gamry Reference System. The potentiodynamic polarization test was performed using a three electrode cell, where the reference electrode was Saturated Calomel SCE, the counter electrode was platinum electrode and the working electrode was the specimens. An open circuit potential with a frequency range of 10^5–0.01 Hz was adopted for the Electrochemical Impedance Spectroscopy and potentiodynamic polarization was carried out at a scan rate of 0.5 mV/s initiated at −250 mV below the open-circuit potential (OCP). Three samples were examined for each sheet.

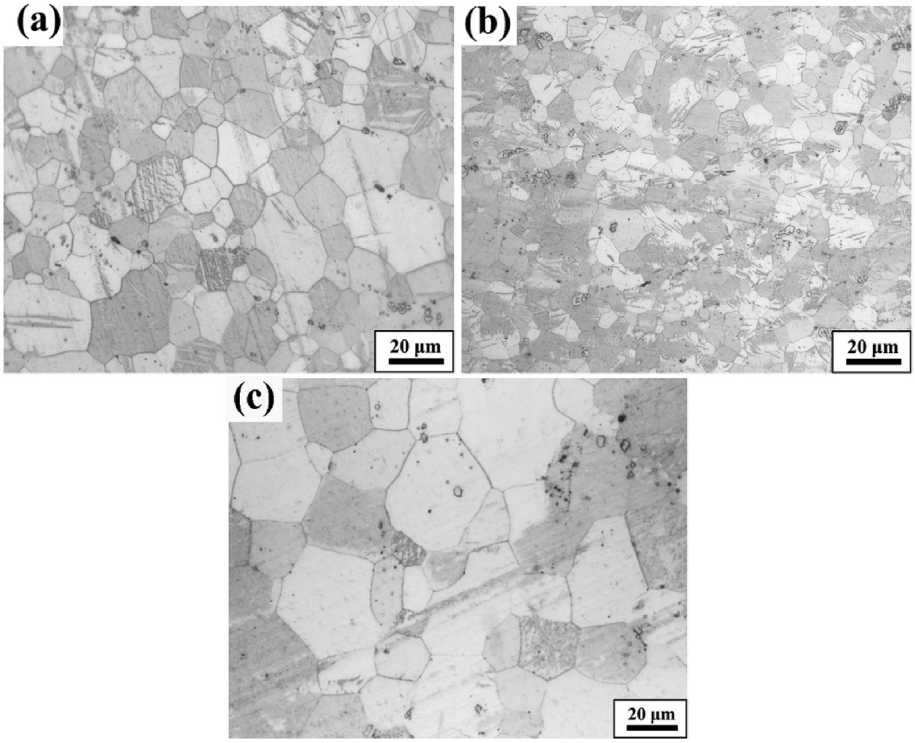

Fig. 2. Optical microscopic image of (a) rolled, (b) stamped and (c) HT-stamped Mg–2Zn-0.5Nd alloy.

3. Results

3.1. Microstructure characterization

Fig. 2 Presents the microstructure of Mg–2Zn-0.5Nd (ZN20) alloys. The optical metallographic images reveal that the grain size of the Mg–2Zn-0.5Nd reduce from 11.3 μm to 5.9 μm after stamping. The grains of the stamped samples were mostly deformed with the presence of twins. After annealing treatment, the grain size increases rapidly to 19.6 μm because of static recrystallization as shown in Figs. 2c and 3(c). Fig. 3 presents the EBSD data of the three samples. Fig. 3a-c presents the inverse pole figure maps of the rolled, stamped and HT-stamped samples. The colors in the grains in the map correspond to the crystallographic axes of the grains in the stereographic triangle or inverse pole figure. The colors in the stereographic triangle reveals that for the rolled and HT-stamped samples, the exposed crystallographic planes of most grains are basal planes while the stamped sample is an even combination of the basal, prism and pyramidal planes (Fig. 3a and b). There is twin activation spread across the grains after stamping due to the induced compressive deformation. Fig. 4a-b shows the {0001} pole figures of rolled and stamped samples. From the figure it is observed that although all three samples exhibit basal texture, but the texture component is significantly different. For the rolled sample, the normal direction (ND) of the basal planes in most grains is perpendicular to the rolling surface, but in some grains the basal plane is deflected to the rolling direction (RD). For the stamped samples, most basal planes are nearly perpendicular to the ND, but there are still some basal planes nearly perpendicular to the RD and transverse direction (TD). As for HT-stamped samples, almost all the basal planes are nearly perpendicular to the ND. The maximum intensity of the basal plane is 11.79, 8.45 and 15.16 for the rolled, stamped and HT-stamped samples, respectively. The XRD further confirms the maximum intensity of the basal plane {0001} (Fig. 5d). The misorientation angle distribution (MAD) shows three significant peaks at 40°, 56° and 86° (Fig. 5e). Nave and Barnett [44] reported that the peaks corresponding to misorientation angles of 30–40, 55–60 and 85–90 can be attributed to the presence of $\{10\bar{1}1\}$ – $\{10\bar{1}2\}$ double twins, $\{10\bar{1}1\}$ compression twin and $\{10\bar{1}2\}$ tension twin. The peak at 86° for the stamped sample being stronger than the rolled and HT-stamped sample further confirms the twin volume fraction is much higher in the stamped sample (Fig. 2).

3.2. Biodegradation property

3.2.1. Immersion tests

The pH variation of the Hank's solution for the rolled, stamped and HT-stamped sample as a function of immersion time is shown in Fig. 6a. The lower pH exhibited by the HT-stamped sample as compared to the rolled and stamped sample indicates a lower corrosion rate. In the early stage, just after immersion, all the samples reacted rapidly with the solution and large amounts of OH^- anions were generated, causing the pH values to increase sharply reaching approximately to 10.5 after 24 h. However, as the reactions progressed and the solutions refreshed the pH value of the samples stabilize due to the balance between the matrix dissolution and the formation of protective film. The HT-stamped Mg–2Zn-0.5Nd sheet exhibited a lower degradation rate with the lowest pH value in Hank's solution.

Fig. 6b presents the corrosion rate of the rolled, stamped and HT-stamped Mg–2Zn-0.5Nd Sheet after immersion in Hank's solution for 14 days. The average corrosion rate for the rolled, stamped and HT-stamped sample after 14 days in vitro immersion are 0.2 mm/year, 0.5 mm/year and 0.15 mm/year respectively.

Within the 14 days immersion period, the corrosion rate of Mg–2Zn-0.5Nd alloys could be ranked as follows: Stamped ZN20 > Rolled ZN20 > HT-stamped ZN20.

3.2.2. Electrochemical test

The electrochemical polarization curves of the specimen after immersion in simulated body fluid (SBF) solution is shown in Fig. 7. Similar trends of both cathodic and anodic polarization curves were obtained for rolled, stamped and HT-stamped sample. The corrosion potential (E_{corr}), corrosion current density (i_{corr}) and the corrosion rate of rolled and stamped alloy extracted by tafel fitting from the

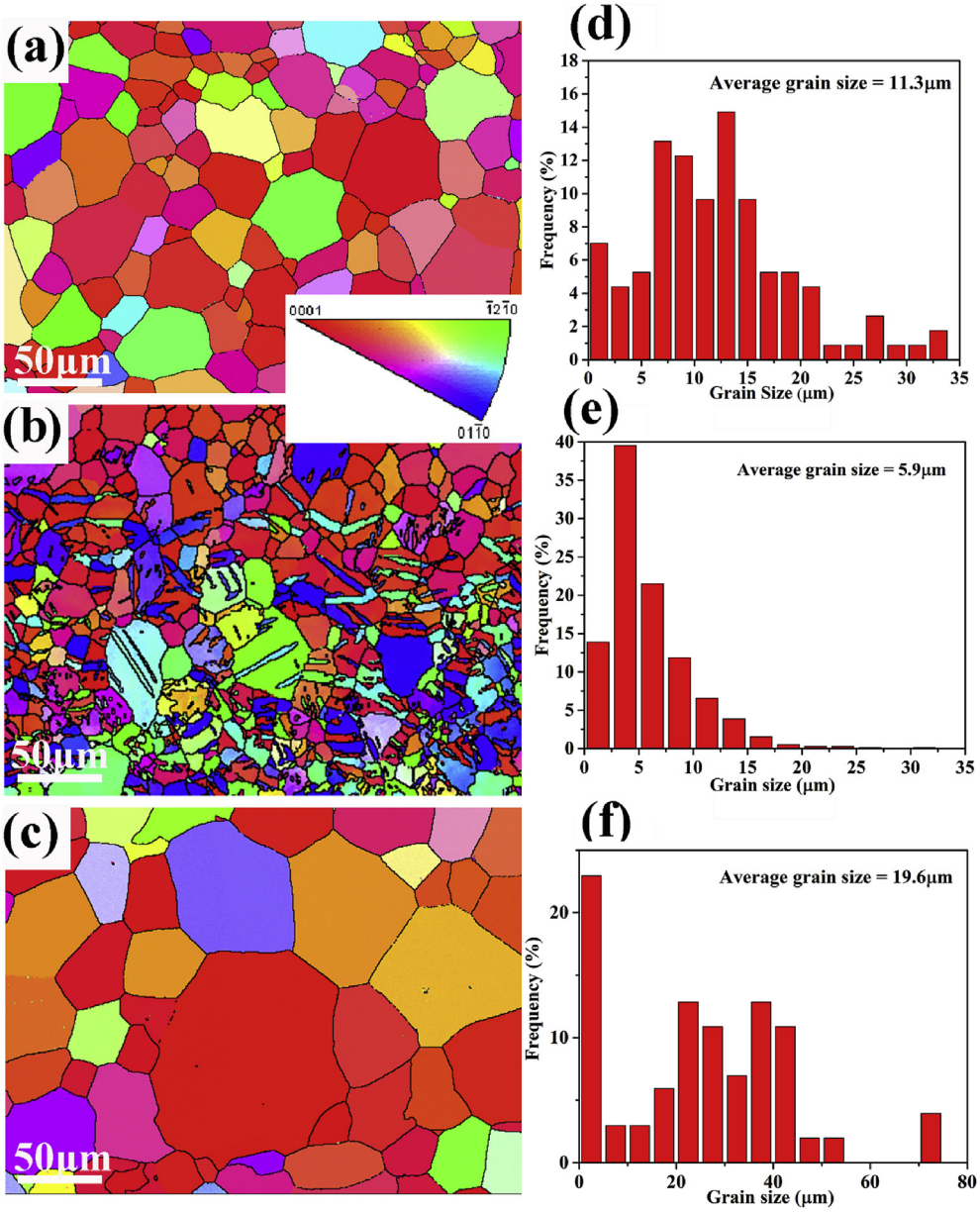

Fig. 3. EBSD orientation maps and the grain structure of the (a) rolled (b) stamped and (c) HT-stamped samples; Grain size distribution of the (d) rolled (e) stamped and (f) HT-stamped samples; stereographic triangle or inverse pole figure reflecting the orientation relationship between the sample surfaces and crystallographic planes of grains.

polarization curve (Fig. 7) are presented in Table 2. It can be observed that the HT-stamped sample exhibited a more positive corrosion potential, lower current density and corrosion rate than the rolled and stamped sample. This shows that stamping process can greatly increase the corrosion rate of Mg–2Zn-0.5Nd (ZN20).

Fig. 8 presents the EIS spectra for the rolled, stamped and HT-stamped ZN20 alloy. It can be seen that the diameter of the capacitive loop for the HT-stamped sample was larger than the rolled and stamped sample. The high frequency behavior of EIS is related to the corrosion rate. A larger diameter of the capacitive loop implies a better corrosion resistance [45]. Therefore, the HT-stamped ZN20 with the largest diameter of high frequency capacitive loop has the best corrosion resistance. The degradation behavior of the rolled, stamped and HT-stamped ZN20 alloy was further analyzed by fitting the EIS spectra result using Zimpfit software. The equivalent circuit and model of the EIS spectra was obtained as shown in Fig. 8. R_s represents the solution resistance. CPE_1 and CPE_2 are the constant phase elements in parallel with the resistive elements. R_1 represents the charge transfer resistance associated with micro-galvanic event. R_2 is the film resistance above the micro-galvanic event, and L indicates the associated inductive element. R_1 and CPE_1 are used to describe the first capacitive loop at high frequency [46]. In general, the higher the value of R_1, the lower the degradation rate of the Mg matrix. According to Table 3 which indicates the fitting result, the value of R_1 decrease in the order; HT-Stamped > Rolled > Stamped ZN20 implying an increase in the degradation rate.

3.2.3. Corrosion morphology

Fig. 9 presents the corrosion morphologies of the ZN20 alloys after immersion in Hank's solution for 14 days. The surfaces of the ZN20 sheets were covered with corrosion products. All three samples suffered a similar corrosion attack, but the magnitude of this attack was different. Fig. 9 (d–f) presents the corrosion surface morphology of the Mg alloy ZN20 sheets after 14 days immersion in Hank's solution and after

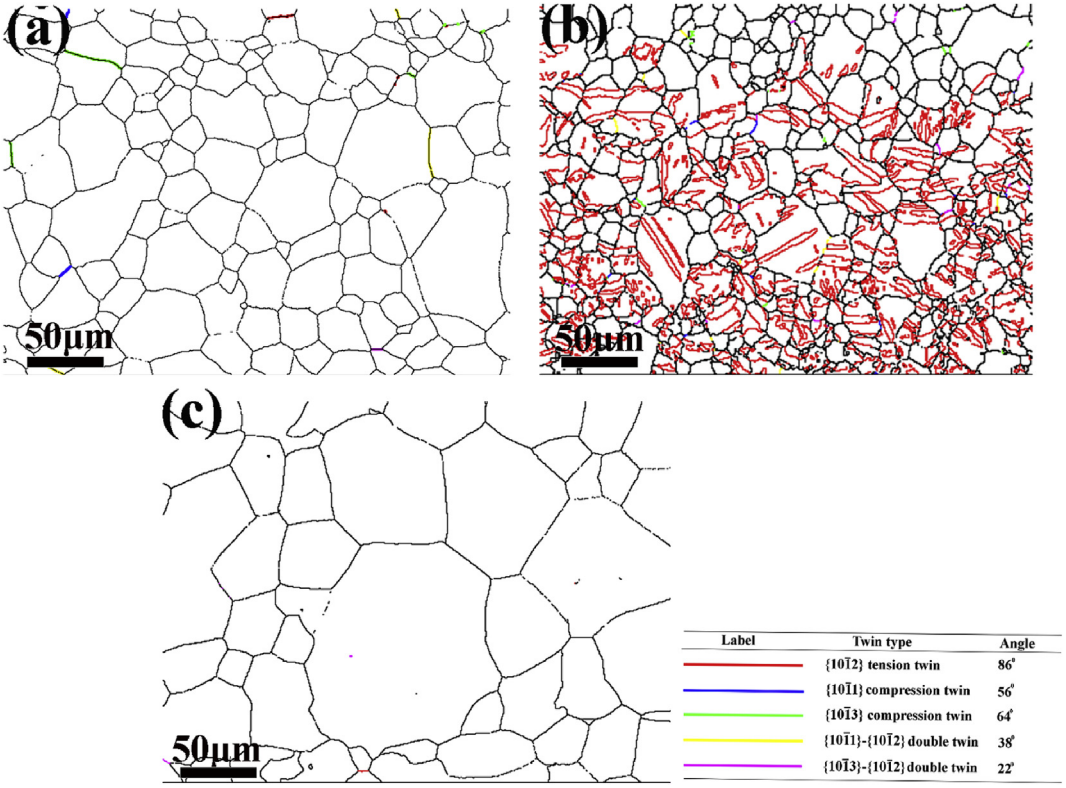

Fig. 4. Grain and twin boundary map of (a) rolled and (b) stamped and (c) HT-stamped Mg–2Zn-0.5Nd alloy.

removal of corrosion products. The surfaces of the specimens were covered by relatively shallow pits. The stamped sample suffered greater corrosion attack with larger and deeper pits, in comparison to the rolled and HT-stamped. After annealing, the stamped ZN20 alloy exhibited few uniformly distributed shallow pits. The larger and deeper pits in the stamped sample and the shallower pits in the HT-stamped sample were in agreement with the highest and lowest mass loss rankings, respectively. Fig. 9a-c presents the macro surface features of the corroded areas of ZN20 alloy after immersion in Hank's solution for 14 days and after removal of corrosion products. The stamped sample was severely corroded. Corrosion penetrated into the specimen interior. In contrast, there were few obvious deep pits on the surface of the rolled Sample.

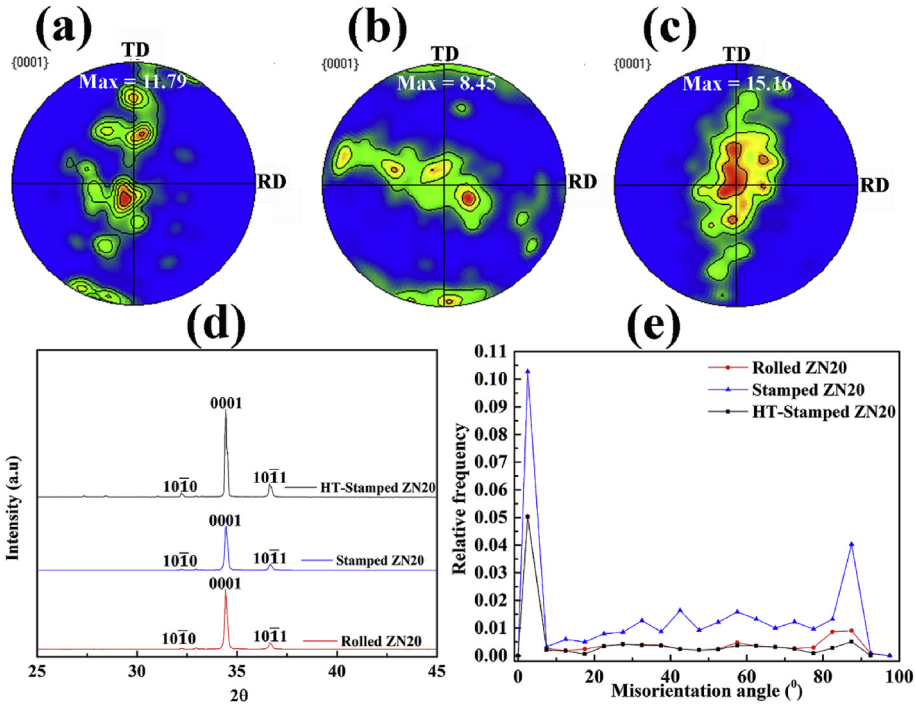

Fig. 5. 0001 pole figures of the (a) rolled (b) stamped (c) HT-stamped samples; (e) XRD patterns and (f) distribution of misorientation angle between grain boundaries for Mg–2Zn-0.5Nd (ZN20).

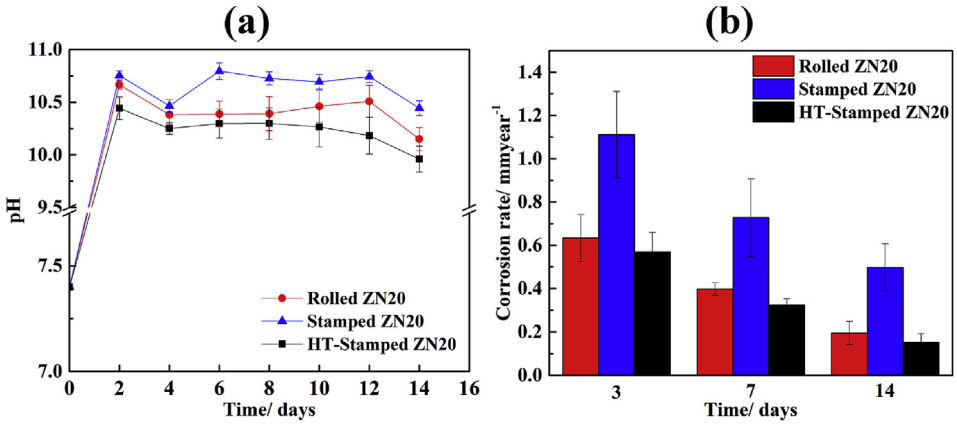

Fig. 6. The pH value (a) and corrosion rate (b) of the rolled, stamped and HT-stamped Mg–2Zn-0.5Nd alloys at different immersion time in Hank's solution at 37 °C.

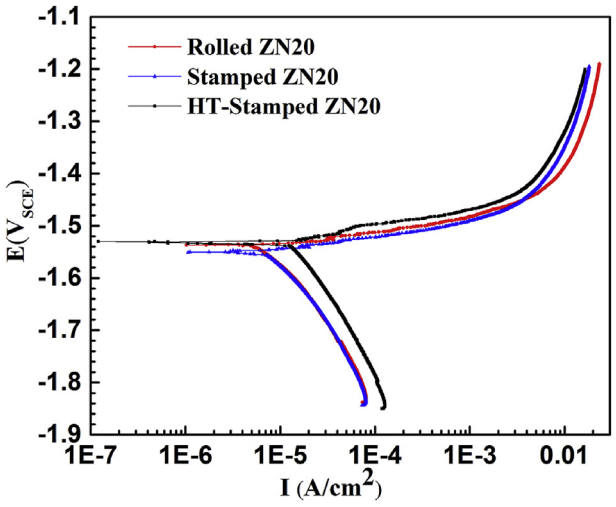

Fig. 7. Potentiodynamic polarization curves of the rolled, stamped and HT-stamped Mg–2Zn-0.5Nd alloys in Hank's solution.

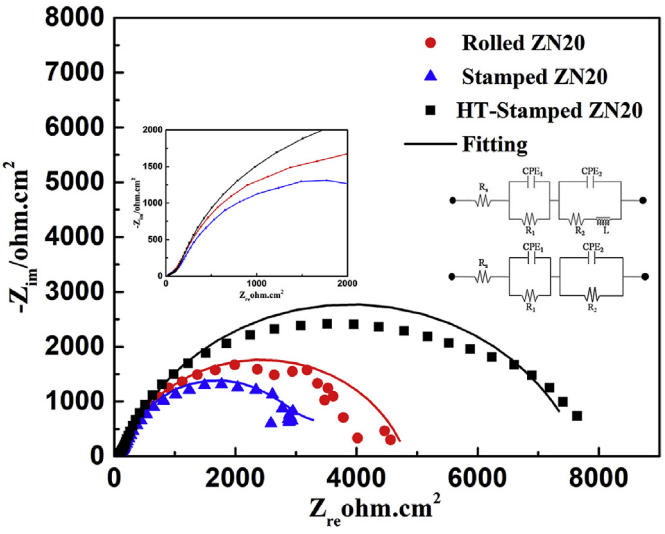

Fig. 8. Nyquist curves and Equivalent Circuit of rolled, stamped and HT-stamped ZN20 in Hank's solution at 37 °C.

Table 2
Electrochemical data extracted from polarization curve.

Alloy	Potential E_{corr} (V vs. SCE)	Current density i_{corr} (μA/cm^2)	Corrosion rate (mm/year)
Rolled ZN20	−1.54 ± 0.02	8.50 ± 0.50	0.194 ± 0.017
Stamped ZN20	−1.55 ± 0.02	12.85 ± 0.25	0.293 ± 0.004
HT-Stamped ZN20	−1.53 ± 0.02	3.94 ± 0.35	0.090 ± 0.030

Corrosion of the HT-stamped sample was less severe. The corrosion morphology also indicated a ranking of the corrosion severity similar to that from the polarization curves and mass loss measurements. The EDS results (Fig. 10d–f) reveal that the surface corrosion products (rectangular area in Fig. 10 a-c) were rich in O, Mg, Zn, Nd, P and Ca. The corrosion product on the rolled sample is less loose as compared to the Stamped sample while the HT-stamped sample has a more compact corrosion product layer.

4. Discussion

Results of OM, EBSD and XRD analysis indicate that there were changes in crystallographic texture, twinning activity and grain size of the rolled ZN20 alloy after stamping. After the Stamping process these three factors, i.e. texture, twinning and grain size, influenced the corrosion rate of ZN20 alloy.

In Mg alloy the {0001} basal plane has a better corrosion resistance than the $\{10\bar{1}0\}$ and $\{11\bar{2}0\}$ prism planes due to the closely packed plane having a higher binding energy and thus lower surface energy [27]. Fig. 4b shows that the basal intensity of the HT-stamped sample is higher than the rolled and stamped sample. Based on this, the corrosion rate of the HT-stamped sample is less than the rolled and stamped sample because it contains a larger fraction of {0001} oriented grain than the rolled and stamped sample. Also, since the theoretical dissociation rates of prism planes $\{10\bar{1}0\}$ and $\{1\bar{1}20\}$ are about 18–20 times higher than that of the {0001} basal plane [27], corrosion could easily occur in the $\{10\bar{1}0\}$ and $\{11\bar{2}0\}$ oriented grains as compared with the {0001} oriented grains. Song et al. reported that the corrosion resistance of the basal planes is much better than that of the prism planes, the rolling surface of the AZ31 plates consisting of mainly basal planes is more corrosion resistant than its cross-section surface composing of mainly prism planes [27].

The grain size of the rolled ZN20 decreases after stamping. Several studies have investigated the influence of grain size on the corrosion of Mg alloys [47–49]. Some studies indicate that grain boundary act as crystallographic defects and this facilitates the corrosion of Mg alloys [50,51]. Others suggest that grain boundaries acts as corrosion barrier and can retard corrosion kinetics [52,53]. In this current work, the stamped sample with the smallest grain size had the highest degradation rate which is consistent with the hypothesis of grain boundaries as crystallographic defects that facilitate corrosion. This is because the

Table 3
Tafel fitting result of ZN20 alloys immersed in Hank's solution.

Alloy	R_s (Ω cm^2)	CPE_1		R_1 (Ω cm^2)	CPE_2		R_2 (Ω cm^2)	L (H cm^{-2})
		Y_{01} (S·sec^n/cm^2)	n_1		Y_{02} (S·sec^n/cm^2)	n_2		
Rolled ZN20	21.46	2.161e-5	0.73	8.827e3	6.518e-6	0.73	94.30	0.1845
Stamped ZN20	21.05	2.209e-5	0.77	7.768e3	1.510e-5	0.67	71.14	0.1424
HT-Stamped ZN20	25.85	1.980e-5	0.80	9.610e3	1.012e-6	0.72	141.18	–

smaller grain size in the stamped ZN20 sheet contained more grain boundaries (Fig. 2). These grain boundaries with high density dislocations contain increased energy and after room temperature deformation, the twin areas around the grain boundary become very reactive and are more vulnerable to galvanic corrosion.

Also, the twin volume fraction of stamped sample is higher than that of the rolled and HT-stamped sample (Figs. 2–4), thus the degradation is more severe on the stamped sample compared to other samples (Fig. 9). The orientation of $\{10\bar{1}2\}$ tension twins can lead to a reorientation of 86.3^0 of the crystal lattice with respect to the untwined Mg matrix [54–56]. The effect of twinning on the corrosion performance can be ascribed to galvanic corrosion due to difference in the crystallographic orientation between the twinned and untwined areas. Additionally, Aung and Zhou [48] demonstrated that corrosion can occur widely in the twinned areas of a strong basal textured AZ31 sheet. The misorientation angle distribution (Fig. 5e) after the Stamping process indicates an initial increase in misorientation from low to high angles. The high frequency at low angle was from low angle grain boundary caused by slip. As observed in Fig. 5e, the high frequency near 86^0 is from $\{10\bar{1}2\}$ tension twinning. This implies that the stamping process induces compressive deformation that is characterized by twins. These twins act as initiation sites to corrosion activity and were detrimental to the corrosion resistance of stamped ZN20 sheets. Zheng et al. reported that the corrosion rate of Mg–Zn alloy increases distinctly after tensile or compressive deformation [57]. Based on the above reason, it can be seen that the corrosion performance of stamped Mg–2Zn-0.5Nd alloy is not only dependent on the grain size and intensity degree of crystallographic orientation for most grains but also the $\{10\bar{1}2\}$ tension twinning plays a vital role. The result suggests the existence of twins could accelerate the corrosion rate of stamped Mg–2Zn-0.5Nd sheet. However, after annealing treatment no obvious deep corrosion pits were observed because lattice defects within the grains were recovered with disappearance of twinning activity and the corrosion resistance of ZN20 was increased. This study reveals that stamping technology followed by annealing treatment can be used as a simple and economic method for the processing of biodegradable Mg alloys implants with small and complex shape.

5. Conclusion

The biodegradable behavior Rolled Mg–2Zn-0.5Nd (ZN20) sheet after stamping process was investigated and the following conclusions were made:

(i) The corrosion rate of the Mg–2Zn-0.5Nd (ZN20) sheet in Hank's solution decreases in the following order: Stamped ZN20 > Rolled ZN20 > HT-Stamped ZN20.
(ii) The maximum intensity of basal {0001} plane had a significant effect on the corrosion rate of rolled Mg–2Zn-0.5Nd (ZN20) sheet after stamping process.
(iii) The high density twin boundaries formed from the activation of the $\{10\bar{1}2\}$ tension twin in combination with the grain boundaries act as initiation site to corrosion attack thereby reducing the corrosion resistance of the rolled Mg–2Zn-0.5Nd (ZN20) sheet after Stamping process.
(iv) Annealing treatment is an appropriate optimization process for diminishing the residual stress and offers promising approach to improving the corrosion resistance of biomedical Mg alloy after stamping.

CRediT authorship contribution statement

Iniobong P. Etim: Conceptualization, Methodology, Investigation, Formal analysis, Writing - original draft. **Wen Zhang:** Validation, Resources. **Lili Tan:** Supervision, Writing - review & editing. **Ke Yang:** Project administration, Funding acquisition.

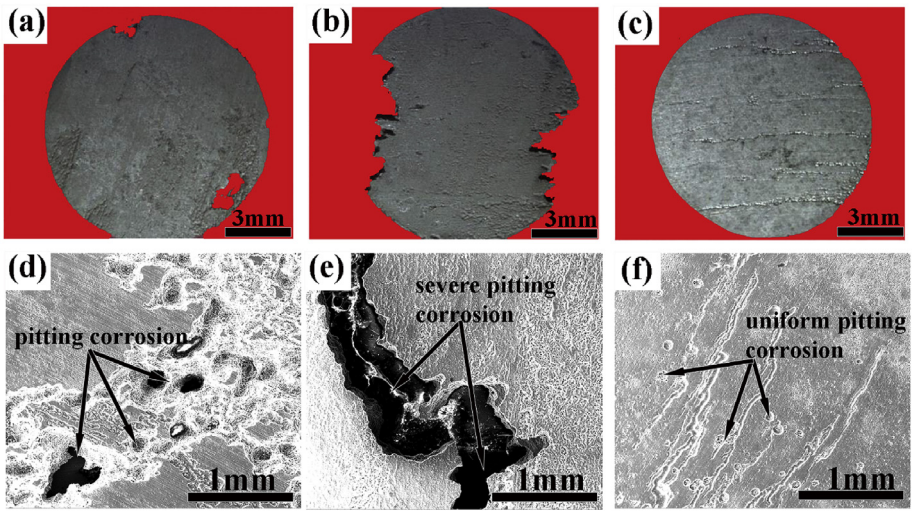

Fig. 9. (a, b, c) Macro-structures and (c, d, e) Micro-structures morphology of the rolled (a, d), stamped (b, e) and HT-stamped (c, f) samples after immersion in Hank's solution for 14 days.

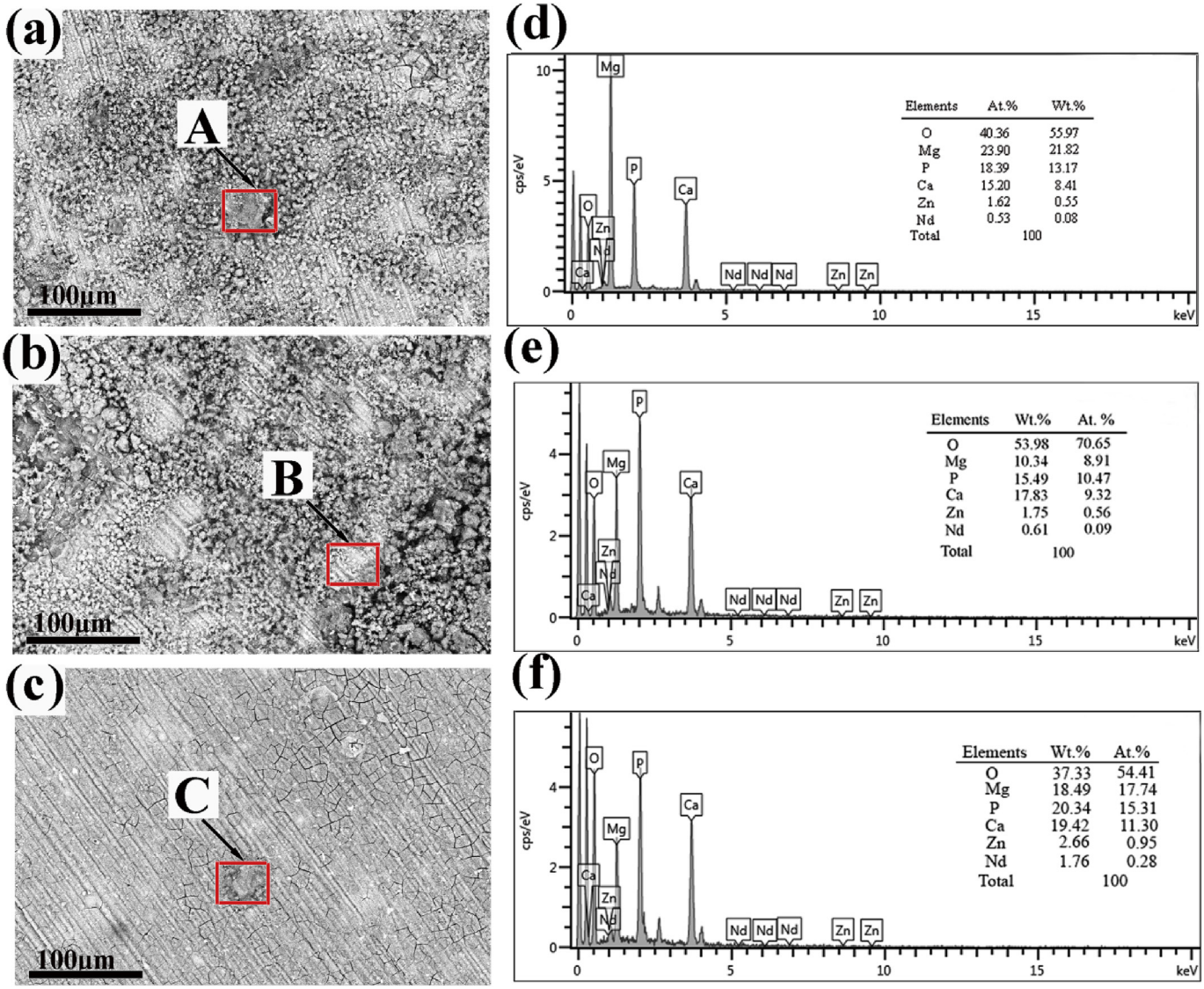

Fig. 10. The corrosion morphologies of the alloy after 14 days immersion in Hank's solution. (a, b, c) Micro-structures of the Rolled, Stamped and HT-stamped sample, (d, e, f) EDS analysis of the areas marked area A and B respectively after 7 days immersion in Hank's solution.

Declaration of competing interest

The authors declare that there are no conflicts of interest.

Acknowledgement

This research was supported by the Key Program of China on Biomedical Materials Research and Tissue Organ Replacement (No. 2016YFC1101804, 2016YFC1100604), funding from Shenyang key R & D and technology transfer program (NO.Z18-0-027) and National Natural Science Foundation of China (No. 51801220).

References

[1] F. Witte, N. Hort, C. Vogt, S. Cohen, K.U. Kainer, R. Willumeit, F. Feyerabend, Degradable biomaterials based on magnesium corrosion, Curr. Opin. Solid State Mater. Sci. 12 (2008) 63–72.
[2] X.N. Gu, Y.F. Zheng, A review on magnesium alloys as biodegradable materials, Front. Mater. Sci. China 4 (2010) 111–115.
[3] F. Witte, H. Ulrich, C. Palm, E. Willbold, Biodegradable magnesium scaffolds: Part II: Peri-implant bone remodeling, J. Biomed. Mater. Res. 81A (2007) 757–765.
[4] N.T. Kirkland, M.P. Staiger, D. Nisbet, C.H.J. Davies, N. Birbilis, Performance-driven design of Biocompatible Mg alloys, JOM (J. Occup. Med.) 63 (2011) 28–34.
[5] E. Zhang, L. Yang, Microstructure, mechanical properties and bio-corrosion properties of Mg–Zn–Mn–Ca alloy for biomedical application, Mater. Sci. Eng., A 497 (2008) 111–118.
[6] S. Zhang, X. Zhang, C. Zhao, J. Li, Y. Song, C. Xie, H. Tao, Y. Zhang, Y. He, Y. Jiang, Research on an Mg-Zn alloy as a degradable biomaterial, Acta Biomater. 6 (2010) 626.
[7] X. Zhang, G. Yuan, Z. Wang, Mechanical properties and biocorrosion resistance of Mg-Nd-Zn-Zr alloy improved by cyclic extrusion and compression, Mater. Lett. 74 (2012) 128–131.
[8] H.S. Brar, J. Wong, M.V. Manuel, Investigation of the mechanical and degradation properties of Mg-Sr and Mg-Zn-Sr alloys for use as potential biodegradable implant materials, J. Mech. Behav. Biomed. Mater. 7 (2012) 87–95.
[9] E. Zhang, W. He, H. Du, K. Yang, Microstructure, mechanical properties and corrosion properties of Mg–Zn–Y alloys with low Zn content, Mater. Sci. Eng., A 488 (2008) 102–111.
[10] F. Witte, V. Kaese, H. Haferkamp, E. Switzer, A. Meyerlindenberg, C.J. Wirth, H. Windhagen, In vivo corrosion of four magnesium alloys and the associated bone response, Biomaterials 26 (2005) 3557–3563.
[11] B. Smola, L. Joska, V. Březina, I. Stulíková, F. Hnilica, Microstructure, corrosion resistance and cytocompatibility of Mg–5Y–4Rare Earth–0.5Zr (WE54) alloy, Mater. Sci. Eng. C 32 (2012) 659–664.
[12] L. Mao, G. Yuan, S. Wang, J. Niu, G. Wu, W. Ding, A novel biodegradable Mg–Nd–Zn–Zr alloy with uniform corrosion behavior in artificial plasma, Mater. Lett. 88 (2012) 1–4.
[13] J.M. Seitz, R. Eifler, J. Stahl, M. Kietzmann, F.W. Bach, Characterization of MgNd2 alloy for potential applications in bioresorbable implantable devices, Acta Biomater. 8 (2012) 3852–3864.
[14] Q. Peng, X. Li, N. Ma, R. Liu, H. Zhang, Effects of backward extrusion on mechanical and degradation properties of Mg-Zn biomaterial, J. Mech. Behav. Biomed. Mater.

10 (2012) 128–137.
[15] A. Drynda, N. Deinet, N. Braun, M. Peuster, Rare earth metals used in biodegradable magnesium-based stents do not interfere with proliferation of smooth muscle cells but do induce the upregulation of inflammatory genes, J. Biomed. Mater. Res. 91A (2009) 360–369.
[16] F. Feyerabend, J. Fischer, J. Holtz, F. Witte, R. Willumeit, H. Drücker, C. Vogt, N. Hort, Evaluation of short-term effects of rare earth and other elements used in magnesium alloys on primary cells and cell lines ☆, Acta Biomater. 6 (2010) 1834–1842.
[17] H.W. Shi, F.C. Liu, E.H. Han, Improving corrosion resistance of epoxy coatings modified with silane monomers on AZ31D magnesium alloy, Canad. Metall. Q. 51 (2013) 485–490.
[18] H.R. Bakhsheshi-Rad, E. Hamzah, M. Daroonparvar, R. Ebrahimi-Kahrizsangi, M. Medraj, In-vitro corrosion inhibition mechanism of fluorine-doped hydroxyapatite and brushite coated Mg–Ca alloys for biomedical applications, Ceram. Int. 40 (2014) 7971–7982.
[19] Y. Nakamura, Y. Tsumura, Y. Tonogai, T. Shibata, Y. Ito, Differences in behavior among the chlorides of seven rare earth elements administered intravenously to rats, Fund. Appl. Toxicol. 37 (1997) 106–116.
[20] C.D. Yim, J. Yang, S.K. Woo, H.-Y. Ha, B.S. You, The effects of microstructural factors on the corrosion behaviour of Mg–5Sn–xZn (x = 1, 3wt%) extrusions, Corrosion Sci. 90 (2015) 597–605.
[21] M.I. Jamesh, G. Wu, Y. Zhao, D.R. McKenzie, M.M.M. Bilek, P.K. Chu, Electrochemical corrosion behavior of biodegradable Mg–Y–RE and Mg–Zn–Zr alloys in Ringer's solution and simulated body fluid, Corrosion Sci. 91 (2015) 160–184.
[22] X.B. Chen, D.R. Nisbet, R.W. Li, P.N. Smith, T.B. Abbott, M.A. Easton, D.H. Zhang, N. Birbilis, Controlling initial biodegradation of magnesium by a biocompatible strontium phosphate conversion coating, Acta Biomater. 10 (2014) 1463–1474.
[23] X.B. Chen, N. Birbilis, T.B. Abbott, A simple route towards a hydroxyapatite–Mg(OH)2 conversion coating for magnesium, Corrosion Sci. 53 (2011) 2263–2268.
[24] F. Cao, Z. Shi, G.-L. Song, M. Liu, M.S. Dargusch, A. Atrens, Influence of hot rolling on the corrosion behavior of several Mg–X alloys, Corrosion Sci. 90 (2015) 176–191.
[25] D. Orlov, K.D. Ralston, N. Birbilis, Y. Estrin, Enhanced corrosion resistance of Mg alloy ZK60 after processing by integrated extrusion and equal channel angular pressing, Acta Mater. 59 (2011) 6176–6186.
[26] G.-L. Song, Z. Xu, Crystal orientation and electrochemical corrosion of polycrystalline Mg, Corrosion Sci. 63 (2012) 100–112.
[27] G.-L. Song, R. Mishra, Z. Xu, Crystallographic orientation and electrochemical activity of AZ31 Mg alloy, Electrochem. Commun. 12 (2010) 1009–1012.
[28] G.-L. Song, Z. Xu, Effect of microstructure evolution on corrosion of different crystal surfaces of AZ31 Mg alloy in a chloride containing solution, Corrosion Sci. 54 (2012) 97–105.
[29] Z. Pu, G.L. Song, S. Yang, J.C. Outeiro, O.W. Dillon, D.A. Puleo, I.S. Jawahir, Grain refined and basal textured surface produced by burnishing for improved corrosion performance of AZ31B Mg alloy, Corrosion Sci. 57 (2012) 192–201.
[30] M. Liu, D. Qiu, M.-C. Zhao, G. Song, A. Atrens, The effect of crystallographic orientation on the active corrosion of pure magnesium, Scripta Mater. 58 (2008) 421–424.
[31] F. Cao, Z. Shi, G.-L. Song, M. Liu, A. Atrens, Corrosion behaviour in salt spray and in 3.5% NaCl solution saturated with Mg(OH)2 of as-cast and solution heat-treated binary Mg–X alloys: X = Mn, Sn, Ca, Zn, Al, Zr, Si, Sr, Corrosion Sci. 76 (2013) 60–97.
[32] M. Liu, P.J. Uggowitzer, A.V. Nagasekhar, P. Schmutz, M. Easton, G.-L. Song, A. Atrens, Calculated phase diagrams and the corrosion of die-cast Mg–Al alloys, Corrosion Sci. 51 (2009) 602–619.
[33] M.-C. Zhao, M. Liu, G. Song, A. Atrens, Influence of the β-phase morphology on the corrosion of the Mg alloy AZ91, Corrosion Sci. 50 (2008) 1939–1953.
[34] G. Song, A. Atrens, M. Dargusch, Influence of microstructure on the corrosion of diecast AZ91D, Corrosion Sci. 41 (1998) 249–273.
[35] T. Abu Leil, N. Hort, W. Dietzel, C. Blawert, Y. Huang, K.U. Kainer, K.P. Rao, Microstructure and corrosion behavior of Mg-Sn-Ca alloys after extrusion, Trans. Nonferrous Metals Soc. China 19 (2009) 40–44.
[36] R. Xin, B. Li, L. Li, Q. Liu, Influence of texture on corrosion rate of AZ31 Mg alloy in 3.5wt.% NaCl, Mater. Des. 32 (2011) 4548–4552.
[37] R. Xin, Y. Luo, A. Zuo, J. Gao, Q. Liu, Texture effect on corrosion behavior of AZ31 Mg alloy in simulated physiological environment, Mater. Lett. 72 (2012) 1–4.
[38] C.R. Mccall, M.A. Hill, R.S. Lillard, Crystallographic pitting in magnesium single crystals, Br. Corrosion J. 40 (2013) 337–343.
[39] R.S. Lillard, G.F. Wang, M.I. Baskes, The role of metallic bonding in the crystallographic pitting of magnesium, ECS Trans. 153 (2006) S251.
[40] K. Hagihara, M. Okubo, M. Yamasaki, T. Nakano, Crystal-orientation-dependent corrosion behaviour of single crystals of a pure Mg and Mg-Al and Mg-Cu solid solutions, Corrosion Sci. 109 (2016) 68–85.
[41] B. Wang, D. Xu, J. Dong, W. Ke, Effect of texture on biodegradable behavior of an as-extruded Mg–3%Al–1%Zn alloy in phosphate buffer saline medium, J. Mater. Sci. Technol. 32 (2016) 646–652.
[42] B.J. Wang, D.K. Xu, J.H. Dong, W. Ke, Effect of the crystallographic orientation and twinning on the corrosion resistance of an as-extruded Mg–3Al–1Zn (wt.%) bar, Scripta Mater. 88 (2014) 5–8.
[43] Y. Zong, G. Yuan, X. Zhang, L. Mao, J. Niu, W. Ding, Comparison of biodegradable behaviors of AZ31 and Mg–Nd–Zn–Zr alloys in Hank's physiological solution, Mater. Sci. Eng., B 177 (2012) 395–401.
[44] M.D. Nave, M.R. Barnett, Microstructures and textures of pure magnesium deformed in plane-strain compression, Scripta Mater. 51 (2004) 881–885.
[45] A. Zomorodian, M.P. Garcia, T. Moura e Silva, J.C.S. Fernandes, M.H. Fernandes, M.F. Montemor, Biofunctional composite coating architectures based on polycaprolactone and nanohydroxyapatite for controlled corrosion activity and enhanced biocompatibility of magnesium AZ31 alloy, Mater. Sci. Eng. C 48 (2015) 434–443.
[46] Y. Song, E.H. Han, D. Shan, D.Y. Chang, B.S. You, The effect of Zn concentration on the corrosion behavior of Mg– x Zn alloys, Corrosion Sci. 65 (2012) 322–330.
[47] J.W. Seong, W.J. Kim, Development of biodegradable Mg–Ca alloy sheets with enhanced strength and corrosion properties through the refinement and uniform dispersion of the Mg2Ca phase by high-ratio differential speed rolling, Acta Biomater. 11 (2015) 531–542.
[48] N.N. Aung, W. Zhou, Effect of grain size and twins on corrosion behaviour of AZ31B magnesium alloy, Corrosion Sci. 52 (2010) 589–594.
[49] K.D. Ralston, N. Birbilis, Effect of grain size on corrosion: a review, Corrosion 66 (2010) 075005-075005-075013.
[50] G.-L. Song, Z. Xu, The surface, microstructure and corrosion of magnesium alloy AZ31 sheet, Electrochim. Acta 55 (2010) 4148–4161.
[51] T. Zhang, Y. Shao, G. Meng, Z. Cui, F. Wang, Corrosion of hot extrusion AZ91 magnesium alloy: I-relation between the microstructure and corrosion behavior, Corrosion Sci. 53 (2011) 1960–1968.
[52] G.R. Argade, S.K. Panigrahi, R.S. Mishra, Effects of grain size on the corrosion resistance of wrought magnesium alloys containing neodymium, Corrosion Sci. 58 (2012) 0-151.
[53] M. Alvarez-Lopez, M.D. Pereda, J.A. del Valle, M. Fernandez-Lorenzo, M.C. Garcia-Alonso, O.A. Ruano, M.L. Escudero, Corrosion behaviour of AZ31 magnesium alloy with different grain sizes in simulated biological fluids, Acta Biomater. 6 (2010) 1763–1771.
[54] D.K. Xu, L. Liu, Y.B. Xu, E.H. Han, The relationship between macro-fracture modes and roles of different deformation mechanisms for the as-extruded Mg–Zn–Zr alloy, Scripta Mater. 58 (2008) 1098–1101.
[55] Q. Jin, S.-Y. Shim, S.-G. Lim, Correlation of microstructural evolution and formation of basal texture in a coarse grained Mg–Al alloy during hot rolling, Scripta Mater. 55 (2006) 843–846.
[56] M.H. Yoo, Slip, twinning, and fracture in hexagonal close-packed metals, Metall. Trans. A 12 (1981) 409–418.
[57] Y. Zheng, Y. Li, J. Chen, Z. Zou, Effects of tensile and compressive deformation on corrosion behaviour of a Mg–Zn alloy, Corrosion Sci. 90 (2015) 445–450.
[58] JunLei Li, Study on Biodegradable Mg-2Zn-0.5Nd Alloys and Optimization Design for Coronary Stent [D]. Shenyang, Institute of Metal Research, 2015.